Visualization and Quantum Control of Light-Accelerated Condensates by Terahertz Multi-dimensional Coherent Spectroscopy

Martin Mootz[1], Liang Luo[2], Jigang Wang[2], and llias E. Perakis[*1]

[1]*Department of Physics, University of Alabama at Birmingham, Birmingham, AL 35294-1170, USA*
[2] *Department of Physics and Astronomy, Iowa State University and Ames Laboratory-U.S. DOE, Ames, IA 50011, USA*

Supplementary Note 1: Gauge-invariant Density Matrix

To study the Multi-Dimensional Coherent Terahertz (MDC-THz) spectra, including light-wave acceleration non-linear quantum transport effects, of superconducting (SC) systems, we consider the real space Bogolubov–de Gennes Hamiltonian of s-wave superconductors [S1, S2]

$$H = \sum_\alpha \int \mathrm{d}^3\mathbf{x}\, \psi_\alpha^\dagger(\mathbf{x}) \left[\varepsilon(\mathbf{p} + e\mathbf{A}(\mathbf{x}, t)) - \mu - e\phi(\mathbf{x}, t) + \mu_\mathrm{H}(\mathbf{x}) + \mu_\mathrm{F}^\alpha(\mathbf{x}) \right] \psi_\alpha(\mathbf{x})$$
$$- \int \mathrm{d}^3\mathbf{x} \left[\Delta(\mathbf{x})\psi_\uparrow^\dagger(\mathbf{x})\psi_\downarrow^\dagger(\mathbf{x}) + \mathrm{h.c.} \right] . \tag{S1}$$

Here, $\psi_\alpha^\dagger(\mathbf{x})$ and $\psi_\alpha(\mathbf{x})$ are the electron creation and annihilation operators with spin index α. The SC complex order parameter is $\Delta(\mathbf{x}) = -2\,g\langle\psi_\downarrow(\mathbf{x})\psi_\uparrow(\mathbf{x})\rangle = |\Delta(\mathbf{x})|\mathrm{e}^{\mathrm{i}\theta(\mathbf{x})}$, where g is the effective electron–electron pairing interaction and $\theta(\mathbf{x})$ is the phase. The energy band dispersion is $\varepsilon(\mathbf{p})$, where $\mathbf{p} = -\mathrm{i}\nabla_\mathbf{x}$ ($\hbar{=}1$) is the momentum operator; $-e$ is the electron charge and μ denotes the equilibrium chemical potential. The Fock energy $\mu_\mathrm{F}^\alpha(\mathbf{x})$ ensures charge conservation, while the Hartree energy $\mu_\mathrm{H}(\mathbf{x})$ moves the phase mode of the SC order parameter above the QP continuum [S2]. Excitation by THz electromagnetic fields is described by the direct coupling of the vector potential $\mathbf{A}(\mathbf{x}, t)$ and the scalar potential $\phi(\mathbf{x}, t)$.

The coherent dynamics is analyzed by using the gauge-invariant density-matrix theory of Ref. [S2]. In addition to the Anderson pseudo-spin precession treated by BCS pseudo-spin models, we include quantum transport, condensate acceleration and spatial variation contributions to the THz nonlinear response. All of the above contributions are treated by using a transformed Wigner function which, unlike for the original density matrix, is invariant under gauge transformation [S2]:

$$\tilde{\rho}(\mathbf{k}, \mathbf{R}) = \int \mathrm{d}^3\mathbf{r} \exp\left[-\mathrm{i}e \int_0^{\frac{1}{2}} \mathrm{d}\lambda\, \mathbf{A}(\mathbf{R} + \lambda\,\mathbf{r}, t) \cdot \mathbf{r}\, \sigma_3 \right]$$
$$\times \langle \Psi^\dagger(\mathbf{R} + \frac{\mathbf{r}}{2}) \Psi(\mathbf{R} - \frac{\mathbf{r}}{2})) \rangle$$
$$\times \exp\left[-\mathrm{i}e \int_{-\frac{1}{2}}^0 \mathrm{d}\lambda\, \mathbf{A}(\mathbf{R} + \lambda\,\mathbf{r}, t) \cdot \mathbf{r}\, \sigma_3 \right] \mathrm{e}^{-\mathrm{i}\mathbf{k}\cdot\mathbf{r}} . \tag{S2}$$

Here, $\Psi(\mathbf{x}) = (\psi_\uparrow(\mathbf{x}), \psi_\downarrow^\dagger(\mathbf{x}))^T$ is the field operator in Nambu space and σ_3 is the Pauli spin matrix. $\mathbf{R} = (\mathbf{x} + \mathbf{x}')/2$ and $\mathbf{r} = \mathbf{x} - \mathbf{x}'$ are the Cooper pair center-of-mass and relative coordinates, respectively.

The non-equilibrium coherent dynamics of superconductors is traditionally described by using the pseudo-spin formalism first introduced by Anderson in Ref. [S3]. Here, the pseudo-spin operators are not related to the physical spin operators. Instead, up and down pseudo-spins correspond to filled and empty electronic $\mathbf{k}$-states. Canted (tilted) spins describe a quantum superposition of up and down pseudo-spin states. To make the connection with previously used pseudo-spin models, we expand the gauge-invariant density matrix Eq. (S2) in terms of pseudo-spin operators defined at every $\mathbf{k}$-point similar to the standard qubit analysis [S3]:

$$\tilde{\rho}(\mathbf{k}, \mathbf{R}) = \sum_{n=0}^3 \tilde{\rho}_n(\mathbf{k}, \mathbf{R})\sigma_n , \tag{S3}$$

where σ_n, $n = 1 \cdots 3$, are the Pauli spin matrices, σ_0 is the unit matrix, and $\tilde{\rho}_n(\mathbf{k}, \mathbf{R})$ define the pseudo-spin components, which here also depend on the condensate center-of-mass spatial coordinate $\mathbf{R}$.

For the purposes of this article, we have expanded the full spatially-dependent equations of motion derived in Ref. [S2] by assuming a weak $\mathbf{R}$-dependence relative to the Cooper pair size. This expansion can be truncated whenever the characteristic length for the spatial variation of the SC condensate (center-of-mass) is larger than the coherence length of the Cooper pair (relative motion). Here, we assume a weak spatial dependence and neglect all terms of order $\mathcal{O}(\nabla_\mathbf{R} \cdot \nabla_\mathbf{k})$ and higher in the gradient expansion, which is a reasonable approximation for BCS s-wave superconductors. For simplicity, we also neglected the Hartree potential, whose effect on the nonlinear response is small for weak spatial dependence. By eliminating the order parameter phase via a gauge transformation [S2], we obtain a set of gauge-invariant coupled equations of motion which describe a nonlinearly driven moving condensate

quantum state with time-dependent center-of-mass momentum $\mathbf{p}_S(t)$ [S2]:

$$\partial_t \tilde{\rho}_0(\mathbf{k}) = -e\mathbf{E} \cdot \nabla_{\mathbf{k}} \tilde{\rho}_3(\mathbf{k}) + |\Delta| \left[\tilde{\rho}_2(\mathbf{k} + \mathbf{p}_S/2) - \tilde{\rho}_2(\mathbf{k} - \mathbf{p}_S/2) \right],$$

$$\partial_t \tilde{\rho}_1(\mathbf{k}) = -\left[\varepsilon(\mathbf{k} - \mathbf{p}_S/2) + \varepsilon(\mathbf{k} + \mathbf{p}_S/2) + 2\mu_{\text{eff}}(t) + 2\mu_F(t) \right] \tilde{\rho}_2(\mathbf{k}),$$

$$\partial_t \tilde{\rho}_2(\mathbf{k}) = \left[\varepsilon(\mathbf{k} - \mathbf{p}_S/2) + \varepsilon(\mathbf{k} + \mathbf{p}_S/2) + 2\mu_{\text{eff}}(t) + 2\mu_F(t) \right] \tilde{\rho}_1(\mathbf{k})$$
$$+ |\Delta| \left[\tilde{\rho}_3(\mathbf{k} + \mathbf{p}_S/2) + \tilde{\rho}_3(\mathbf{k} - \mathbf{p}_S/2) - \tilde{\rho}_0(\mathbf{k} - \mathbf{p}_S/2) + \tilde{\rho}_0(\mathbf{k} + \mathbf{p}_S/2) \right],$$

$$\partial_t \tilde{\rho}_3(\mathbf{k}) = -e\mathbf{E} \cdot \nabla_{\mathbf{k}} \tilde{\rho}_0(\mathbf{k}) - |\Delta| \left[\tilde{\rho}_2(\mathbf{k} + \mathbf{p}_S/2) + \tilde{\rho}_2(\mathbf{k} - \mathbf{p}_S/2) \right], \tag{S4}$$

where

$$|\Delta| = -2g \sum_{\mathbf{k}} \tilde{\rho}_1(\mathbf{k}) \tag{S5}$$

is the time-dependent SC order parameter amplitude. For a homogeneous system, the effective chemical potential

$$\mu_{\text{eff}}(t) = e\,\phi(t) + \frac{1}{2}\frac{\partial}{\partial t}\theta(t) - \mu \tag{S6}$$

is determined by the time-dependent SC order parameter phase $\theta(t)$ and scalar potential $\phi(t)$, while the superfluid momentum $\mathbf{p}_S(t)$ resulting from Cooper pair acceleration by the light-wave electric field is given by [S2]

$$\partial_t \mathbf{p}_S(t) = 2\,e\,\mathbf{E}(t) \quad \rightarrow \quad \mathbf{p}_S(t) = -2\,e\,\mathbf{A}(t). \tag{S7}$$

We now compare the above equations of motion to previously studied Anderson pseudo-spin models. Unlike for the latter BCS models, here Eq. (S4) is gauge invariant. It is determined by the order parameter amplitude $|\Delta(t)|$, which remains real at all times in our calculation. The dynamics of the order parameter phase $\theta(t)$ modifies the effective potential $\mu_{\text{eff}}(t)$, Eq. (S6). Equation (S4) includes quantum transport terms such as $e\,\mathbf{E} \cdot \nabla_{\mathbf{k}} \tilde{\rho}_3(\mathbf{k})$, which are absent in previous pseudo-spin models and displace the electronic populations in $\mathbf{k}$-space due to condensate acceleration. The coupling between $\tilde{\rho}_0(\mathbf{k})$ and $\tilde{\rho}_3(\mathbf{k})$ in Eq. (S4) arises from inversion symmetry (IS) breaking induced by the field $\mathbf{E}(t)$, whose experimental consequences were studied in [S4–S6]. In the above equations, phase space filling (PSF) contributions arise from the spin-↑ and spin-↓ non-equilibrium electron populations expressed as $\tilde{\rho}_3(\mathbf{k}+\mathbf{p}_S/2)+\tilde{\rho}_0(\mathbf{k}+\mathbf{p}_S/2)$ and $\tilde{\rho}_0(\mathbf{k} - \mathbf{p}_S/2) - \tilde{\rho}_3(\mathbf{k} - \mathbf{p}_S/2)$. These electron populations of the moving condensate non-equilibrium state are displaced in $\mathbf{k}$-space by the time-dependent condensate momentum $\mathbf{p}_S(t)$. Unlike in previously studied Anderson pseudo-spin models, here the THz-time-periodic condensate acceleration couples different pseudo-spins, i.e., couples the density matrices $\tilde{\rho}(\mathbf{k})$ at $\mathbf{k}$ and $\tilde{\rho}(\mathbf{k}\pm\mathbf{p}_S(t)/2)$ at $\mathbf{k}\pm\mathbf{p}_S(t)/2$. For time-periodic driving, such light-induced coupling of the pseudo-spins at different points in momentum space connected by the oscillating condensate momentum leads to Floquet momentum sidebands. For strong $\mathbf{E}, \mathbf{p}_S \neq 0$, the light-induced dynamical breaking of the equilibrium IS described by the above equations can result in symmetry-forbidden harmonics, gapless superconductivity, and quasi-particle quantum phases controlled by strong THz field pulses [S2]. These theoretical predictions were verified experimentally over long time intervals of 100's ps [S4–S6].

To interpret the numerical results obtained by solving the full gauge-invariant equations of motion, we derive a pseudo-spin oscillator model similar to Anderson's original analysis [S3], by taking the second time derivative of Eq. (S4) and using the condensate acceleration Eq. (S7):

$$\partial_t^2 \tilde{\rho}_2(\mathbf{k}) + \left[\varepsilon(\mathbf{k} - \mathbf{p}_S/2) + \varepsilon(\mathbf{k} + \mathbf{p}_S/2) + 2(\mu_{\text{eff}} + \mu_F)\right]^2 \tilde{\rho}_2(\mathbf{k}) + 4|\Delta(t)|^2 \tilde{\rho}_2(\mathbf{k})$$
$$= S_{\mathbf{k}}(t) + \partial_t |\Delta(t)| \left[\tilde{\rho}_3(\mathbf{k} + \mathbf{p}_S/2) + \tilde{\rho}_3(\mathbf{k} - \mathbf{p}_S/2) - \tilde{\rho}_0(\mathbf{k} - \mathbf{p}_S/2) + \tilde{\rho}_0(\mathbf{k} + \mathbf{p}_S/2)\right] + 2\tilde{\rho}_1(\mathbf{k})\,\partial_t\left[\mu_{\text{eff}}(t) + \mu_F(t)\right]. \tag{S8}$$

The above equation describes pseudo-spin oscillators at each different $\mathbf{k}$-point. In equilibrium, similar equations were derived by Anderson [S3] to describe pseudo-spin flips and Higgs collective modes within the random phase approximation. Here, a THz-light-driven rotation of the pseudo-spins away from their equilibrium orientations along the x–z plane leads to time-periodic pseudo-spin y-component modulation, $\tilde{\rho}_2(\mathbf{k}) \neq 0$ ($\tilde{\rho}_2 = 0$ in equilibrium). The last term on the left-hand side (lhs) describes parametric driving of pseudo-spin oscillations by time-dependent changes in the excitation energy gap determined by the time-dependent order parameter amplitude $|\Delta(t)|$.

The right-hand side (rhs) of Eq. (S8) contains three source terms that extend previous works [S7–S9]. The first term is proportional to the laser electric field $\mathbf{E}(t)$:

$$S_{\mathbf{k}}(t) = \tilde{\rho}_1(\mathbf{k})\,e\,\mathbf{E}(t) \cdot \left[\nabla_{\mathbf{k}+\mathbf{p}_S/2}\,\varepsilon(\mathbf{k} + \mathbf{p}_S/2) - \nabla_{\mathbf{k}-\mathbf{p}_S/2}\,\varepsilon(\mathbf{k} - \mathbf{p}_S/2)\right]$$
$$- |\Delta(t)| \left(e\,\mathbf{E}(t) \cdot \nabla_{\mathbf{k}+\mathbf{p}_S/2}\right) \left[\tilde{\rho}_0(\mathbf{k} + \mathbf{p}_S/2) + \tilde{\rho}_3(\mathbf{k} + \mathbf{p}_S/2)\right]$$
$$- |\Delta(t)| \left(e\,\mathbf{E}(t) \cdot \nabla_{\mathbf{k}-\mathbf{p}_S/2}\right) \left[\tilde{\rho}_0(\mathbf{k} - \mathbf{p}_S/2) - \tilde{\rho}_3(\mathbf{k} - \mathbf{p}_S/2)\right]. \tag{S9}$$

In the above equation, the first line corresponds to the previously studied longitudinal pseudo-magnetic field component, which drives Anderson pseudo-spin precession [S7]. The second and third lines are quantum transport terms due to condensate acceleration by $\mathbf{E}(t)$, absent in previous Anderson pseudo-spin models. These terms couple the pseudo-spin at $\mathbf{k}$ with the pseudo-spins at $\mathbf{k} \pm \mathbf{p}_\mathrm{S}/2$. They have the form $\propto e\mathbf{E} \cdot \nabla_\mathbf{k} n_\sigma(\mathbf{k})$, where n_σ, $\sigma = \uparrow, \downarrow$ are the spin-up and spin-down electron populations, and enhance the effects of interest here.

The dynamics of the order parameter amplitude $|\Delta(t)|$ determines the second term on the rhs of Eq. (S8). This order parameter amplitude describes the transverse component of the pseudo-magnetic field [S3] arising from the mean field coupling of the pseudo-spins [S3]. The amplitude dynamics is determined by the equation of motion

$$\partial_t |\Delta(t)| = 2g \sum_{\mathbf{k}'} \left[\varepsilon(\mathbf{k}' + \mathbf{p}_\mathrm{S}/2) + \varepsilon(\mathbf{k}' - \mathbf{p}_\mathrm{S}/2) \right] \tilde{\rho}_2(\mathbf{k}') , \tag{S10}$$

which, similar to Anderson's equilibrium theory [S3], describes the collective effects that characterize a SC state. Such collective behavior arises from the coupling of all $\mathbf{k}$-point pseudo-spins by the pairing interaction. By expanding the above equation of motion to second order in $\mathbf{p}_\mathrm{S}(t)$, we obtain

$$\partial_t |\Delta(t)| = 4g \sum_{\mathbf{k}'} \varepsilon(\mathbf{k}') \, \tilde{\rho}_2(\mathbf{k}') + \frac{g}{2} \sum_{\mathbf{k}'} (\mathbf{p}_\mathrm{S} \cdot \nabla_{\mathbf{k}'})^2 \, \varepsilon(\mathbf{k}') \, \tilde{\rho}_2(\mathbf{k}') + \mathcal{O}(\mathbf{p}_\mathrm{S}^4) , \tag{S11}$$

with initial condition $|\Delta(t = -\infty)| = \Delta_0$. For sufficiently strong time-periodic driving, $\mathbf{p}_\mathrm{S}^2(t)$ on the rhs of Eq. (S11) leads to sidebands of the equilibrium SC excitations, determined by the oscillations of the condensate momentum. As seen from Eq. (S7), these sidebands are found at frequencies determined by the spectrum of $\mathbf{A}^2(t)$, which is peaked at frequencies $\sim 2\omega_\mathrm{p}$. The coherent nonlinear coupling introduced by the $\propto \mathbf{p}_\mathrm{S}^2(t)$ term in Eq. (S11) results in significant enhancement of low-frequency spectral changes in $\Delta(\omega)$ with increasing pump field (Fig. 1). The above driving term is modified by PSF effects as in Eq. (S8), determined by the non-equilibrium electron populations $\tilde{\rho}_0(\mathbf{k}+\mathbf{p}_\mathrm{S}/2)+\tilde{\rho}_3(\mathbf{k}+\mathbf{p}_\mathrm{S}/2)$ and $\tilde{\rho}_0(\mathbf{k}-\mathbf{p}_\mathrm{S}/2)-\tilde{\rho}_3(\mathbf{k}-\mathbf{p}_\mathrm{S}/2)$. Compared to previous Anderson pseudo-spin models [S7–S9], these populations are displaced in momentum space by $\mathbf{p}_\mathrm{S}(t)/2$ due to acceleration of the superconductor into a moving (current-flowing) condensate state with finite center-of-mass momentum. Finally, the last source term on the rhs of Eq. (S8) drives pseudo-spin oscillations due to the time-dependent changes in the effective potential and Fock energy, which depend on the SC order parameter phase dynamics $\frac{\partial^2 \theta(t)}{\partial t^2}$.

Supplementary Note 2: Pump-driven non-equilibrium quantum state

First, we consider the time evolution of the pseudo-spins driven by a single strong pump pulse. We decompose the density matrix $\tilde{\rho}^\mathrm{p}(\mathbf{k})$ describing the pump-driven quantum state as

$$\tilde{\rho}^\mathrm{p}(\mathbf{k}) = \tilde{\rho}^0(\mathbf{k}) + \Delta\tilde{\rho}(\mathbf{k}) , \tag{S12}$$

where $\tilde{\rho}^0(\mathbf{k})$ is the density matrix of the equilibrium state and $\Delta\tilde{\rho}(\mathbf{k})$ describes the pump-induced change. Noting that $\tilde{\rho}_2^0(\mathbf{k}) = 0$ for the stationary superconductor state, we describe the precession of the pseudo-spins away from their equilibrium $x - z$ plane orientations, $\tilde{\rho}_2^\mathrm{p}(\mathbf{k}) = \Delta\tilde{\rho}_2(\mathbf{k})$, by combining Eqs. (S8) and (S10):

$$\partial_t^2 \, \Delta\tilde{\rho}_2(\mathbf{k}) + \left[\varepsilon(\mathbf{k} - \mathbf{p}_\mathrm{S}/2) + \varepsilon(\mathbf{k} + \mathbf{p}_\mathrm{S}/2) + 2(\mu_\mathrm{eff} + \mu_\mathrm{F}) \right]_\mathrm{p}^2 \Delta\tilde{\rho}_2(\mathbf{k}) + 4|\Delta_\mathrm{p}(t)|^2 \Delta\tilde{\rho}_2(\mathbf{k})$$

$$- 2g \left[\tilde{\rho}_3(\mathbf{k} + \mathbf{p}_\mathrm{S}/2) + \tilde{\rho}_3(\mathbf{k} - \mathbf{p}_\mathrm{S}/2) - \tilde{\rho}_0(\mathbf{k} - \mathbf{p}_\mathrm{S}/2) + \tilde{\rho}_0(\mathbf{k} + \mathbf{p}_\mathrm{S}/2) \right]_\mathrm{p} \sum_{\mathbf{k}'} \left[\varepsilon(\mathbf{k}' + \mathbf{p}_\mathrm{s}/2) + \varepsilon(\mathbf{k}' - \mathbf{p}_\mathrm{s}/2) \right]_\mathrm{p} \Delta\tilde{\rho}_2(\mathbf{k}')$$

$$= S_\mathbf{k}^\mathrm{p}(t) . \tag{S13}$$

The above equation of motion extends Anderson's random phase approximation treatment of pseudo-spin canting to the non-perturbative, THz-time-periodic driven superconductor regime [S3]. The field-dependent source term $S_\mathbf{k}^\mathrm{p}(t)$, Eq. (S9), drives the pseudo-spin precession. Our main results here can be captured by neglecting the quantum transport contributions to this driving term, and by expanding the electron band dispersion in powers of the center-of-mass momentum $\mathbf{p}_\mathrm{S}^\mathrm{p}$:

$$S_\mathbf{k}^\mathrm{p}(t) \approx \tilde{\rho}_1^\mathrm{p}(\mathbf{k}) \, (e\,\mathbf{E}^\mathrm{p}(t) \cdot \nabla_\mathbf{k})(\mathbf{p}_\mathrm{S}^\mathrm{p} \cdot \nabla_\mathbf{k}) \, \varepsilon(\mathbf{k}) . \tag{S14}$$

This source term corresponds to the pseudo-magnetic field component along the z-axis considered in previous works [S7, S8]. It describes time-periodic driving of pseudo-spin precession at frequencies $\sim 2\omega_\mathrm{p}$, where ω_p is the pump frequency.
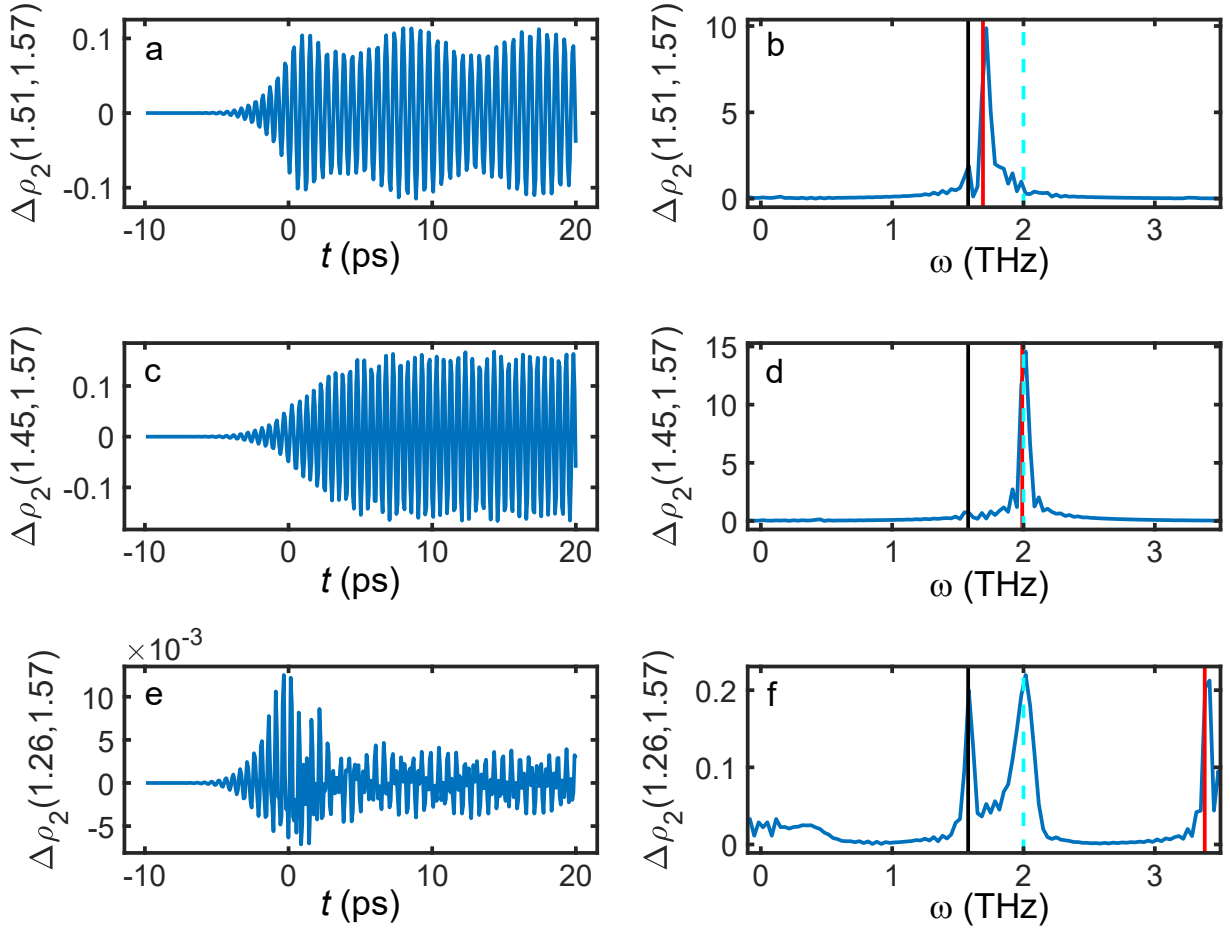
Figure S1. Dynamics and spectra of $\Delta\tilde{\rho}_2(\mathbf{k})$ for different $\mathbf{k}$ pseudo-spins. **a**, **c**, and **e** Dynamics of $\Delta\tilde{\rho}_2(\mathbf{k})$ for 3 different wavevectors $\mathbf{k}$ using a pump peak electric field of $160\,\mathrm{kV\,cm^{-1}}$. **b**, **d**, and **f** The corresponding spectra. The spectra show three main peaks centered at the QP excitation energy (solid red vertical line), the two-photon absorption frequency $\omega = 2\omega_\mathrm{p} \sim 2\Delta_0$ (dashed cyan vertical line), and the Higgs collective mode frequency ω_H (solid black vertical line).

The lhs of Eq. (S13) describes the excitations of the pump-dressed non-equilibrium SC state. This driven state is characterized by time-dependent parameters $|\Delta_\mathrm{p}(t)|$, $\mathbf{p}_\mathrm{S}^\mathrm{p}(t)$, and $\mu_\mathrm{eff}(t)$. The third-order nonlinear response is obtained by approximating these parameters by their equilibrium values, i.e., by setting $\mathbf{p}_\mathrm{S}^\mathrm{p} = 0$, $|\Delta_\mathrm{p}| = \Delta_0$, and $\tilde{\rho}^\mathrm{p}(t) \approx \tilde{\rho}^0$ on the lhs. The solution of Eq. (S13) can then be expressed in terms of a response function [S9, S10], similar to the description of exciton–exciton correlations in semiconductor quantum wells [S11, S12]. This response function, defined by the lhs of Eq. (S13), describes quantum dynamics and memory effects governed by the elementary excitations of the SC system, i.e., by QPs and Higgs collective modes.

Two non-equilibrium effects become important for driving pseudo-spin dynamics in Eq. (S13) for sufficiently strong pump field strengths. First, the ultrafast dynamics of the SC order parameter amplitude $|\Delta_\mathrm{p}(t)|$, which determines the pseudo-spin oscillator frequency. Figure 1 shows that $|\Delta_\mathrm{p}(t)|$ decreases from its equilibrium value during few cycles of light-wave field oscillations, and then fluctuates at longer times around a new asymptotic value $\Delta_\infty < \Delta_0$. This non-instantaneous order parameter dynamics in the pump-dressed system changes the quasi-particle energy gap and the oscillator frequency in Eq. (S13) (third term on the lhs), which results in parametric driving of pseudo-spin oscillations. Second, the coupling of the pseudo-spin (density matrix) at $\mathbf{k}$ with the pseudo-spins at $\mathbf{k} \pm \mathbf{p}_\mathrm{S}/2$ results in Floquet momentum sidebands for strong THz-time-periodic driving.

To interpret our full numerical calculation, the time evolution of the density matrix component $\Delta\tilde{\rho}_2(\mathbf{k})$, which describes pseudo-spin canting from the equilibrium direction driven by a multi-cycle THz-time-periodic pump, is calculated by solving Eq. (S13). The results are shown in Fig. S1 for three different $\mathbf{k}$-point pseudo-spins. With increasing driving field, the asymptotic value of the order parameter of the pump-driven non-equilibrium state,

$\Delta_\infty < \Delta_0$, changes significantly as compared to its equilibrium value. The calculated Fourier transformed $\Delta\rho_2^{\mathrm{p}}(\omega, \mathbf{k})$ then displays three distinct spectral peaks as a function of frequency ω, which depend on $\mathbf{k}$. These three main peaks are centered at (i) the QP excitation energy $E_\mathbf{k} = 2\sqrt{[\varepsilon(\mathbf{k}) + \mu_{\mathrm{eff}} + \mu_{\mathrm{F}}]^2 + |\Delta_\infty|^2}$ (solid red vertical line), (ii) the two-photon absorption frequency $\omega = 2\omega_{\mathrm{p}} \sim 2\Delta_0$ (dashed cyan vertical line), which describes second harmonic generation determined by the time-periodic multi-cycle field, and (iii) the Higgs collective mode frequency $\omega_{\mathrm{H}} = 2\Delta_\infty < 2\Delta_0$ (solid black vertical line). Additional Floquet sidebands are suppressed for the chosen intermediate pump field strengths here. When the QP excitations are resonantly excited by the pump $\mathbf{E}^2$ spectrum, the $\Delta\rho_2^{\mathrm{p}}(\omega, \mathbf{k})$ calculated spectra are dominated by the peak at the QP excitation energy $E_\mathbf{k}$ with $\mathbf{k}$ close to the minimum of the excitation gap, where the density of states is maximum (first panel of Fig. S1). By varying $\mathbf{k}$, the second panel shows a QP peak at the position of the second harmonic generation peak. The last panel shows a QP peak around 3.4 meV, which is weakly excited by the pump pulse. The above variations in the excitation of the different $\mathbf{k}$ Rabi oscillators are due to the change in resonance between the QP excitation energies (pseudo-spin harmonic oscillator frequencies) $E_\mathbf{k}$ and $2\omega_{\mathrm{p}}$ when varying $\mathbf{k}$. Since Fig. S1 shows that the main contribution to the pseudo-spin oscillations comes from QP excitations close to the minimum excitation energy $\sim \omega_{\mathrm{H}}$, where the density of states is enhanced, in the interpretation of the MDC-THz spectral peaks, we use the fact that the dynamics of $\Delta\tilde{\rho}_2(\mathbf{k})$ is dominated by frequencies $\sim \omega_{\mathrm{H}}$ (Higgs or QP excitations, field-dependent) and $\sim 2\omega_{\mathrm{p}}$ (mostly QP excitations, fixed by the laser frequency).

Supplementary Note 3: Phase Coherent Pump–Probe Spectra

To model the MDC-THz coherent nonlinear spectroscopy experiments of particular interest here, we consider the experimental collinear pump–probe geometry of Refs. [S5, S13] first introduced to study semiconductors. A thin SC film is excited by collinearly propagating THz pump and probe pulses arriving at times t_{p} and t_{pro}. The SC response to these two phase-locked pulses is measured by the transmitted E-field $\mathcal{E}_{\mathrm{pp}}(t, \tau)$, which depends on the sampling time t (real time) and on the time delay $\tau = t_{\mathrm{p}} - t_{\mathrm{pro}}$ determining the phase difference between the two driving electromagnetic fields (coherence time). As we discuss below, the important signals at high excitation come from the temporal regime where the two pulses overlap in time. In this case, interference between pump and probe excitations is coherently controlled by tuning τ. For a thin film geometry, we obtain from Maxwell's equations the following expression for the transmitted E-field [S2]:

$$\mathcal{E}(t) = E(t) - \frac{\mu_0 c}{2n} J(t), \tag{S15}$$

where $E(t)$ is the applied electric field, n is the refractive index, and

$$J = 2e \sum_\mathbf{k} \nabla_\mathbf{k} \varepsilon(\mathbf{k}) \, \tilde{\rho}_0(\mathbf{k}) \tag{S16}$$

is the gauge-invariant current. The latter supercurrent is expressed exactly in terms of the gauge-invariant density matrix $\tilde{\rho}$ calculated here, so that the current explicitly obeys the continuity equation [S2]. In terms of the original density matrix ρ, the calculated gauge-invariant density matrix $\tilde{\rho}$ is expressed as

$$
\begin{aligned}
\tilde{\rho}_0(\mathbf{k}) &= \frac{1}{2}\left[\rho_{11}(\mathbf{k} - \mathbf{p}_{\mathrm{S}}/2) + \rho_{22}(\mathbf{k} + \mathbf{p}_{\mathrm{S}}/2)\right] \\
&= \rho_0(\mathbf{k}) + \frac{1}{2}\left[-\frac{\mathbf{p}_{\mathrm{S}}}{2} \cdot \nabla_\mathbf{k}\rho_{11}(\mathbf{k}) + \frac{\mathbf{p}_{\mathrm{S}}}{2} \cdot \nabla_\mathbf{k}\rho_{22}(\mathbf{k})\right] + \mathcal{O}(\mathbf{p}_{\mathrm{S}}^2) \\
&\approx \rho_0(\mathbf{k}) - \frac{1}{2}\mathbf{p}_{\mathrm{S}} \cdot \nabla_\mathbf{k}\rho_3(\mathbf{k}),
\end{aligned}
\tag{S17}
$$

which reproduces previous results [S7, S8] after expansion of the full results obtained here.

The MDC-THz spectra are determined by calculating the Fourier transformation of the nonlinear differential transmission, after subtracting from the response to two phase-coherent pulses the nonlinear responses to the individual pump and probe pulses. In this way, we obtain the correlated nonlinear signal

$$\mathcal{E}_{\mathrm{NL}}(t, \tau) = \mathcal{E}_{\mathrm{pp}}(t, \tau) - \mathcal{E}_{\mathrm{p}}(t, \tau) - \mathcal{E}_{\mathrm{pro}}(t), \tag{S18}$$

where $\mathcal{E}_{\mathrm{pp}}(t, \tau)$ is the transmitted field for excitation by both pulses and $\mathcal{E}_{\mathrm{pro}}(t)$ and $\mathcal{E}_{\mathrm{p}}(t, \tau)$ are the transmitted fields for excitation by the probe ($t_{\mathrm{pro}} = 0$) and pump ($t_{\mathrm{p}} = \tau$) fields alone. It is important to note that the above

correlated signal cannot be interpreted in terms of the nonlinear response to a single pulse. Instead, it comes from coupled excitations by two pulses, whose relative phase is controlled by the time delay τ. The MDC-THz spectra are determined by the two-dimensional Fourier transformation $\mathcal{E}_{\mathrm{NL}}(\omega)$, where $\omega = (\omega_t, \omega_\tau)$ is the 2D "frequency vector". A well-defined phase difference between pump and probe results in sharp peaks along the vertical ω_τ-axis.

As seen from Eqs. (S15) and (S16), the experimentally measured correlated nonlinear signal Eq. (S18) is determined by the dynamics of $\Delta\tilde{\rho}_0(\mathbf{k}) = \tilde{\rho}_0^{\mathrm{pp}}(\mathbf{k}) - \tilde{\rho}_0^{\mathrm{p}}(\mathbf{k}) - \tilde{\rho}_0^{\mathrm{pro}}(\mathbf{k})$, where the density matrix $\tilde{\rho}^{\mathrm{pp}}(\mathbf{k})$ describes the quantum state driven by both pump and probe phase-coherent pulses, and $\tilde{\rho}^{\mathrm{p}}(\mathbf{k})$ ($\tilde{\rho}^{\mathrm{pro}}(\mathbf{k})$) describes the state excited by the pump (probe) field alone. We consider a strong narrowband pump pulse with spectrum centered at $\omega_{\mathrm{p}} = (\omega_0, -\omega_0)$ (Fig. 1b). To simplify the interpretation of the numerical results and to resonantly drive both Higgs and quasiparticle excitations, we consider here a weaker broadband probe pulse with frequencies $\omega_{\mathrm{pro}} = (\omega_0 \pm \Delta\omega_{\mathrm{pro}}, 0)$, where $\Delta\omega_{\mathrm{pro}}$ denotes the frequency width (Fig. 1b). Similar to previous studies in semiconductors [S11, S12, S14], the nonlinear signal measured in the experiment can then be interpreted by considering the linear response of the pump-driven quantum state, described by the density matrix $\tilde{\rho}^{\mathrm{p}}$, to a weak probe:

$$\tilde{\rho}^{\mathrm{pp}}(\mathbf{k}) = \tilde{\rho}^{\mathrm{p}}(\mathbf{k}) + \delta\tilde{\rho}^{\mathrm{pp}}(\mathbf{k}), \tag{S19}$$

where the probe induces the change $\delta\tilde{\rho}^{\mathrm{pp}}$ in the pump-driven non-equilibrium state. The latter is obtained from the following equation of motion, linearized in terms of the probe, which determines the photocurrent Eq. (S16):
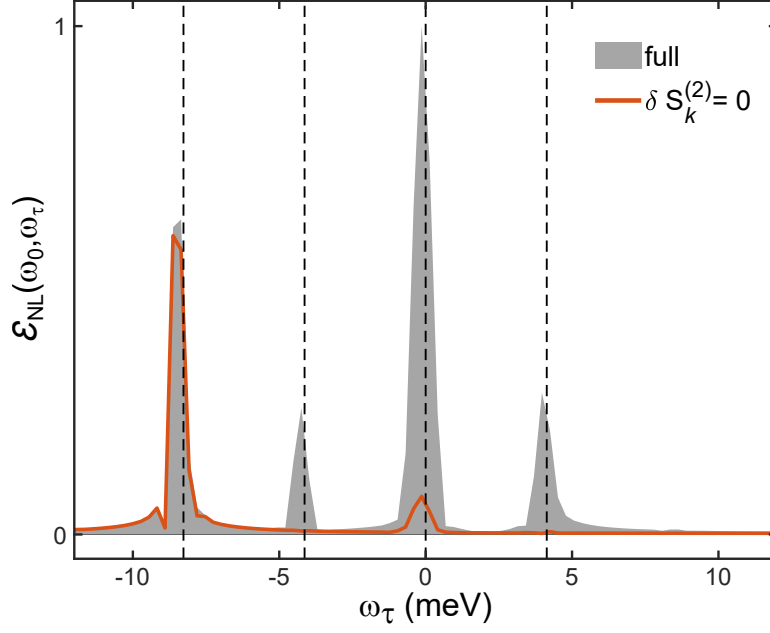
$$\begin{aligned}
\partial_t \delta\tilde{\rho}_0^{\mathrm{pp}}(\mathbf{k}) =& \frac{1}{2}|\Delta_{\mathrm{p}}(t)|\mathbf{p}_{\mathrm{S}}^{\mathrm{pro}} \cdot \left[\nabla_{\mathbf{k}+\mathbf{p}_{\mathrm{S}}^{\mathrm{p}}/2}\Delta\tilde{\rho}_2^{\mathrm{p}}(\mathbf{k}+\mathbf{p}_{\mathrm{S}}^{\mathrm{p}}/2) + \nabla_{\mathbf{k}-\mathbf{p}_{\mathrm{S}}^{\mathrm{p}}/2}\,\Delta\tilde{\rho}_2^{\mathrm{p}}(\mathbf{k}-\mathbf{p}_{\mathrm{S}}^{\mathrm{p}}/2)\right] \\
& - e\mathbf{E}_{\mathrm{pro}} \cdot \nabla_{\mathbf{k}}\tilde{\rho}_3^{\mathrm{p}}(\mathbf{k}) - e\mathbf{E}_{\mathrm{p}} \cdot \nabla_{\mathbf{k}}\delta\tilde{\rho}_3^{\mathrm{pp}}(\mathbf{k}) \\
& + |\Delta_{\mathrm{p}}(t)|\left[\delta\tilde{\rho}_2^{\mathrm{pp}}(\mathbf{k}+\mathbf{p}_{\mathrm{S}}^{\mathrm{p}}/2) - \delta\tilde{\rho}_2^{\mathrm{pp}}(\mathbf{k}-\mathbf{p}_{\mathrm{S}}^{\mathrm{p}}/2)\right] \\
& + \delta\Delta_{\mathrm{pp}}(t)\left[\Delta\tilde{\rho}_2^{\mathrm{p}}(\mathbf{k}+\mathbf{p}_{\mathrm{S}}^{\mathrm{p}}/2) - \Delta\tilde{\rho}_2^{\mathrm{p}}(\mathbf{k}-\mathbf{p}_{\mathrm{S}}^{\mathrm{p}}/2)\right] + \mathcal{O}([\mathbf{p}_{\mathrm{S}}^{\mathrm{pro}}]^2).
\end{aligned} \tag{S20}$$

The above equation extends previous nonlinear results in a gauge-invariant way and also treats strong fields and interference effects between pump and probe excitations that overlap in time. There are four terms on the rhs. The first term determines the pump–probe signal calculated in previous works [S9] and does not rely on interference between pump and probe. It contributes when the probe arrives after the pump and does not require any temporal overlap between the two pulses. Our calculations in Fig. 2 show that this term governs the signal for low fields. Noting from Fig. S1 that the frequency components of the pump-driven $\Delta\tilde{\rho}_2^{\mathrm{p}}(\mathbf{k})$ are centered at frequencies $\sim 2\omega_{\mathrm{p}}$ (QP excitations) and $\sim \omega_{\mathrm{H}}$ (Higgs mode or charge density fluctuations close to the SC gap), this term generates MDC-THz peaks at four-wave mixing (FWM) and third harmonic generation (3HG) 2D frequencies, $2\omega_{\mathrm{p}} \pm \omega_{\mathrm{pro}} = (2\omega_0 \pm \omega_0 \pm \Delta\omega_{\mathrm{pro}}, -2\omega_0)$ and $\omega_{\mathrm{H}} \pm \omega_{\mathrm{pro}} = (\omega_{\mathrm{H}} \pm \omega_0 \pm \Delta\omega_{\mathrm{pro}}, -\omega_{\mathrm{H}})$. However, it does not produce the strong CWM peaks discussed in the main text. The second term on the rhs of Eq. (S20) comes from quantum transport effects, which enhance the spectral peaks. However, the main MDC-THz spectral features of interest here come from the last two terms on the rhs of Eq. (S20), which contribute when the pump and probe excitations overlap in time. These contributions are controlled by the phase coherence time τ. The third term is the most important one, described by the equation of motion obtained by linearizing Eq. (S13) with respect to the weak probe without approximation of the strong pump excitation [S11, S12, S14]:

$$\begin{aligned}
\partial_t^2 \delta\tilde{\rho}_2^{\mathrm{pp}}(\mathbf{k}) &+ \left[\varepsilon(\mathbf{k}-\mathbf{p}_{\mathrm{S}}/2) + \varepsilon(\mathbf{k}+\mathbf{p}_{\mathrm{S}}/2) + 2(\mu_{\mathrm{eff}}+\mu_{\mathrm{F}})\right]_{\mathrm{p}}^2 \delta\tilde{\rho}_2^{\mathrm{pp}}(\mathbf{k}) + 4\,|\Delta_{\mathrm{p}}(t)|^2\,\delta\tilde{\rho}_2^{\mathrm{pp}}(\mathbf{k}) \\
&= \delta S_{\mathbf{k}}^{(2)}(t,\tau) - \delta\left[\varepsilon(\mathbf{k}+\mathbf{p}_{\mathrm{S}}/2) + \varepsilon(\mathbf{k}-\mathbf{p}_{\mathrm{S}}/2) + 2(\mu_{\mathrm{eff}}+\mu_{\mathrm{F}})\right]^2 \Delta\tilde{\rho}_2^{\mathrm{p}}(\mathbf{k}) \\
&+ \partial_t\delta|\Delta_{\mathrm{pp}}(t,\tau)|\left[\tilde{\rho}_3(\mathbf{k}+\mathbf{p}_{\mathrm{S}}/2) + \tilde{\rho}_3(\mathbf{k}-\mathbf{p}_{\mathrm{S}}/2) - \tilde{\rho}_0(\mathbf{k}-\mathbf{p}_{\mathrm{S}}/2) + \tilde{\rho}_0(\mathbf{k}+\mathbf{p}_{\mathrm{S}}/2)\right]_{\mathrm{p}} \\
&- 4\,\delta|\Delta_{\mathrm{pp}}(t,\tau)|^2 \Delta\tilde{\rho}_2^{\mathrm{p}}(\mathbf{k}) \\
&+ \partial_t|\Delta_{\mathrm{p}}(t)|\,\delta\left[\tilde{\rho}_3(\mathbf{k}+\mathbf{p}_{\mathrm{S}}/2) + \tilde{\rho}_3(\mathbf{k}-\mathbf{p}_{\mathrm{S}}/2) - \tilde{\rho}_0(\mathbf{k}-\mathbf{p}_{\mathrm{S}}/2) + \tilde{\rho}_0(\mathbf{k}+\mathbf{p}_{\mathrm{S}}/2)\right].
\end{aligned} \tag{S21}$$

In the above equation, the probe-induced fluctuations of the pump-driven order parameter, $\delta|\Delta_{\mathrm{pp}}(t,\tau)| = |\Delta_{\mathrm{pp}}(t,\tau)| - |\Delta_{\mathrm{p}}(t,\tau)|$, are determined by the equation of motion

$$\begin{aligned}
\partial_t\delta|\Delta_{\mathrm{pp}}(t,\tau)| = &\,2g\sum_{\mathbf{k}'}\left[\varepsilon(\mathbf{k}'+\mathbf{p}_{\mathrm{s}}/2) + \varepsilon(\mathbf{k}'-\mathbf{p}_{\mathrm{s}}/2)\right]_{\mathrm{p}}\delta\tilde{\rho}_2^{\mathrm{pp}}(\mathbf{k}') \\
&+ 2g\sum_{\mathbf{k}'}\delta\left[\varepsilon(\mathbf{k}'+\mathbf{p}_{\mathrm{s}}/2) + \varepsilon(\mathbf{k}'-\mathbf{p}_{\mathrm{s}}/2)\right]\Delta\tilde{\rho}_2^{\mathrm{p}}(\mathbf{k}').
\end{aligned} \tag{S22}$$

Figure S2. $\mathcal{E}_{\mathrm{NL}}(\omega)$ as a function of ω_τ at fixed $\omega_t = \omega_0$. The result of the full calculation (shaded area) is compared with the results obtained by switching off $\delta S_{\mathbf{k}}^{(2)}(t)$ (solid line). Vertical dashed lines indicate PP and FWM signals. Unlike for the FWM peak at $\omega_\tau = -2\omega_0$, the PP peak at $\omega_\tau = 0$ is strongly reduced when $\delta S^{(2)} = 0$, which indicates that it mainly comes from sum-frequency Raman processes also discussed before.

Substituting the above equation in Eq. (S21) and using the property $\delta|\Delta_{\mathrm{pp}}(t,\tau)|^2 = 2|\Delta_{\mathrm{p}}(t,\tau)||\delta|\Delta_{\mathrm{pp}}(t,\tau)||$, we obtain

$$\partial_t^2\, \delta\tilde{\rho}_2^{\mathrm{PP}}(\mathbf{k}) + \left[\varepsilon(\mathbf{k}-\mathbf{p}_{\mathrm{S}}/2) + \varepsilon(\mathbf{k}+\mathbf{p}_{\mathrm{S}}/2) + 2(\mu_{\mathrm{eff}}+\mu_{\mathrm{F}})\right]_{\mathrm{p}}^2\, \delta\tilde{\rho}_2^{\mathrm{PP}}(\mathbf{k}) + 4\,|\Delta_{\mathrm{p}}|^2\, \delta\tilde{\rho}_2^{\mathrm{PP}}(\mathbf{k})$$

$$- 2g\left[\tilde{\rho}_3(\mathbf{k}+\mathbf{p}_{\mathrm{S}}/2) + \tilde{\rho}_3(\mathbf{k}-\mathbf{p}_{\mathrm{S}}/2) - \tilde{\rho}_0(\mathbf{k}-\mathbf{p}_{\mathrm{S}}/2) + \tilde{\rho}_0(\mathbf{k}+\mathbf{p}_{\mathrm{S}}/2)\right]_{\mathrm{p}} \sum_{\mathbf{k}'}\left[\varepsilon(\mathbf{k}'+\mathbf{p}_{\mathrm{s}}/2) + \varepsilon(\mathbf{k}'-\mathbf{p}_{\mathrm{s}}/2)\right]_{\mathrm{p}}\, \delta\tilde{\rho}_2^{\mathrm{PP}}(\mathbf{k}')$$

$$= \delta S_{\mathbf{k}}^{(2)}(t,\tau) + \delta S_{\mathbf{k}}^{\mathrm{R}}(t,\tau)$$

$$- 8|\Delta_{\mathrm{p}}|\,\Delta\tilde{\rho}_2^{\mathrm{p}}(\mathbf{k})\,\delta|\Delta_{\mathrm{pp}}(t,\tau)|$$

$$+ \partial_t|\Delta_{\mathrm{p}}|\,\delta\left[\tilde{\rho}_3(\mathbf{k}+\mathbf{p}_{\mathrm{S}}/2) + \tilde{\rho}_3(\mathbf{k}-\mathbf{p}_{\mathrm{S}}/2) - \tilde{\rho}_0(\mathbf{k}-\mathbf{p}_{\mathrm{S}}/2) + \tilde{\rho}_0(\mathbf{k}+\mathbf{p}_{\mathrm{S}}/2)\right]. \tag{S23}$$

The lhs of the above equation describes the response function of the pump-driven system as discussed in the previous section. Below we discuss the role of the different source terms on the rhs of Eq. (S23), which require phase-coherent two-pulse photoexcitation and vanish if we neglect the coupling between excitations by different pulses.

I. Sum-frequency-Raman: Third-Order Responses

We start with the first term on the rhs of Eq. (S23), $\delta S_{\mathbf{k}}^{(2)}(t,\tau) = S_{\mathbf{k}}^{\mathrm{pp}}(t,\tau) - S_{\mathbf{k}}^{\mathrm{p}}(t,\tau)$. This is obtained from Eq. (S9) and determines the third-order response. The dominant two-photon excitation process described by this term depends on the interference between pump and probe fields, controlled by the coherence time τ:

$$\delta S_{\mathbf{k}}^{(2)}(t,\tau) \approx \tilde{\rho}_1^{\mathrm{p}}(\mathbf{k})\,\left[(e\,\mathbf{E}_{\mathrm{p}}\cdot\nabla_{\mathbf{k}})(\mathbf{p}_{\mathrm{S}}^{\mathrm{pro}}\cdot\nabla_{\mathbf{k}}) + (e\,\mathbf{E}_{\mathrm{pro}}\cdot\nabla_{\mathbf{k}})(\mathbf{p}_{\mathrm{S}}^{\mathrm{p}}\cdot\nabla_{\mathbf{k}})\right]\varepsilon(\mathbf{k}). \tag{S24}$$

This source term drives the pseudo-spin oscillators via the sum-frequency Raman process $\omega_{\mathrm{p}} + \omega_{\mathrm{pro}} = (2\omega_0 \pm \Delta\omega_{\mathrm{pro}}, -\omega_0)$. Its contribution to the MDC-THz signal is given by the third term on the rhs of Eq. (S20). This process should be contrasted to the two-photon charge fluctuation processes considered in Ref. [S7, S8]. The latter are induced by the pump field alone and contribute when the probe arrives later, via the first term on the rhs of Eq. (S20), without pump–probe interference. $\delta S^{(2)}$ generates MDC-THz signals at 2D frequencies $\omega_{\mathrm{pro}}+\omega_{\mathrm{p}}-\omega_{\mathrm{p}} = (\omega_0\pm\Delta\omega_{\mathrm{pro}}, 0)$ (pump–probe, PP), and $\omega_{\mathrm{pro}} + \omega_{\mathrm{p}} + \omega_{\mathrm{p}} = (3\omega_0 \pm \Delta\omega_{\mathrm{pro}}, -2\omega_0)$ (pump–probe third-harmonic generation, 3HG). In contrast,
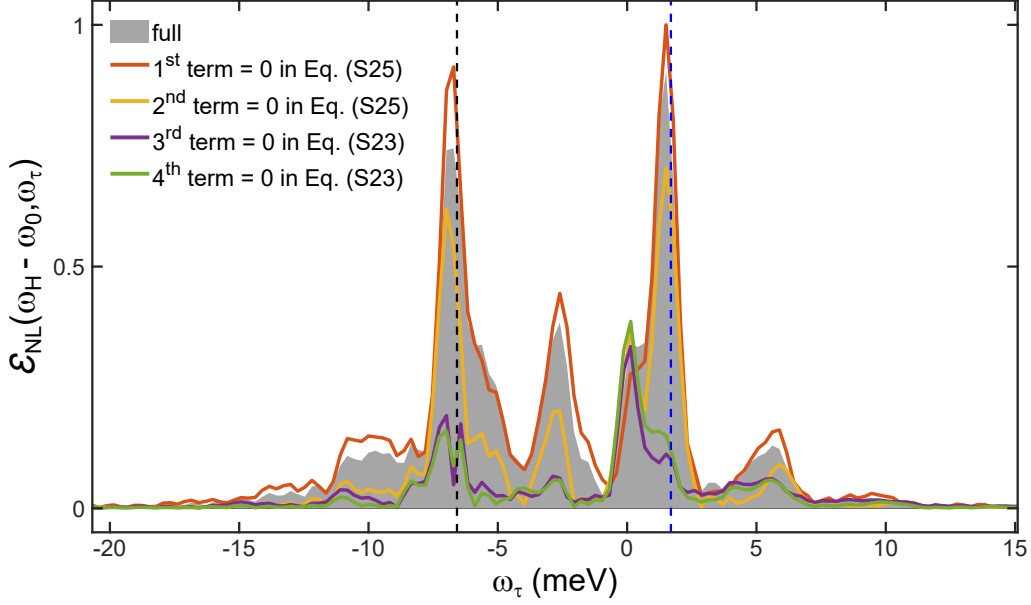
Figure S3. $\mathcal{E}_{NL}(\omega)$ as a function of ω_τ at fixed $\omega_t = \omega_H - \omega_0$. The result of the full calculation (shaded area) is compared with the results obtained by switching off the first term on the rhs of Eq. (S25) (red line), second term on the rhs of Eq. (S25) (orange line), third term on the rhs of Eq. (S23) (purple line), and fourth term on the rhs of Eq. (S23) (green line). CFWM (CPP) peak is indicated by a dashed vertical black (blue) line. Switching off the vertex correction Raman contribution (orange line) reduces the signals, while the non-interacting Raman contribution to Eq. (S25) (red line) only slightly modifies the signals. Most importantly, the correlated wave-mixing signals identified here dominate over third- and fifth-order nonlinear processes discussed before, as seen by the dramatic suppression of the peaks when the parametric driving seventh-order response processes (purple line) proposed here are switched off. The latter higher correlation seventh-order nonlinear processes change the ω_τ spectral profile in a qualitative way, unlike for previously discussed third- and fifth-order conventional Raman processes. These results indicate that, by looking at the slice $\omega_t = \omega_H - \omega_0$ as a function of ω_τ and separating it from the slice $\omega_t = 2\omega_0 - \omega_0$ by increasing the pump driving, we can identify correlated wave-mixing signals arising from light-induced SC correlations, further distinguished from their temperature dependence discussed in the main text.

the two-photon excitations induced by the pump alone contribute at 2D frequencies $2\omega_p - \omega_{pro} = (\omega_0 \pm \Delta\omega_{pro}, -2\omega_0)$ (four-wave mixing, FWM) and $2\omega_p + \omega_{pro} = (3\omega_0 \pm \Delta\omega_{pro}, -2\omega_0)$ (3HG) via the first term on the rhs of Eq. (S20). To distinguish between the above one-pulse and two-pulse two-photon processes, we fix $\omega_t = \omega_0$ and plot in Fig. S2 the calculated $\mathcal{E}_{NL}(\omega)$ as a function of ω_τ. The result of the full calculation (shaded area) is compared with the result obtained by switching off $\delta S^{(2)}$ in Eq. (S23) (solid line). Figure S2 demonstrates two strong peaks, at $\omega_\tau = 0, -2\omega_0$, and two weaker peaks, at $\omega_\tau = \pm\omega_0$. The latter weaker peaks increase with probe field as $\mathcal{O}(\mathbf{E}_{pro}^2)$ and are generated by $\omega_p + \omega_{pro} - \omega_{pro}$ and $\omega_{pro} + \omega_{pro} - \omega_p$ processes. The stronger peaks arise from the PP, $\omega_{pro} + \omega_p - \omega_p$ ($\delta S^{(2)}$) and FWM, $2\omega_p - \omega_{pro}$, processes. FWM and PP are distinguished via ω_τ in Fig. S3. Our numerical results show that, unlike for the peak at $\omega_\tau = -2\omega_0$, the peak at $\omega_\tau = 0$ is strongly reduced when $\delta S^{(2)} = 0$. Figure S2 also shows that the rest of the source terms on the rhs of Eq. (S23) play a minor role at $\omega_\tau = 0$. This $\omega_\tau = 0$ peak reflects the PP process. On the other hand, the peak at $2\omega_p - \omega_{pro}$ is not affected by $\delta S^{(2)}$ and is generated by the FWM process.

We conclude that one can isolate and separate experimentally the different third-order nonlinear response contributions discussed in previous works, by varying the frequency ω_τ corresponding to the coherence time τ while fixing $\omega_t = \omega_0$, the frequency corresponding to the real time t. In particular, by looking at the MDC-THz slice at $\omega_t = \omega_0$, the peak at $\omega_\tau = 0$ arises from sum-frequency Raman processes, which require pump–probe interference ($\delta S^{(2)}$), while the peak at $\omega_\tau = -2\omega_0$ arises from two-photon excitations by the pump pulse alone, which is sensed by a probe pulse arriving later than the pump. All third-order nonlinear processes discussed above and the third-order nonlinear signals, which emerge when the excitation energy gap, $\omega_H = 2\Delta_\infty < 2\omega_0 \sim 2\Delta_0$, shifts with increasing pump field, are summarized in Tables S1 and S2.

II. Difference-Frequency-Raman: Fifth-Order Responses

The second source term on the rhs of Eq. (S23) generates fifth-order SC responses via difference-frequency Raman nonlinear processes with vertex corrections:

$$\delta S_{\mathbf{k}}^{\mathrm{R}}(t,\tau) = -\delta \left[\varepsilon(\mathbf{k}+\mathbf{p}_{\mathrm{S}}/2) + \varepsilon(\mathbf{k}-\mathbf{p}_{\mathrm{S}}/2) + 2(\mu_{\mathrm{eff}} + \mu_{\mathrm{F}})\right]^2 \Delta \tilde{\rho}_2^{\mathrm{p}}(\mathbf{k})$$
$$+ 2g \left[\tilde{\rho}_3(\mathbf{k}+\mathbf{p}_{\mathrm{S}}/2) + \tilde{\rho}_3(\mathbf{k}-\mathbf{p}_{\mathrm{S}}/2) - \tilde{\rho}_0(\mathbf{k}-\mathbf{p}_{\mathrm{S}}/2) + \tilde{\rho}_0(\mathbf{k}+\mathbf{p}_{\mathrm{S}}/2)\right]_{\mathrm{p}} \sum_{\mathbf{k}'} \delta \left[\varepsilon(\mathbf{k}'+\mathbf{p}_{\mathrm{s}}/2) + \varepsilon(\mathbf{k}'-\mathbf{p}_{\mathrm{s}}/2)\right] \Delta \tilde{\rho}_2^{\mathrm{p}}(\mathbf{k}'),$$
$$(S25)$$

where

$$\delta \left[\varepsilon(\mathbf{k}-\mathbf{p}_{\mathrm{S}}/2) + \varepsilon(\mathbf{k}+\mathbf{p}_{\mathrm{S}}/2)\right] = \frac{1}{2}\mathbf{p}_{\mathrm{S}}^{\mathrm{pro}} \cdot \left[\nabla_{\mathbf{k}+\mathbf{p}_{\mathrm{S}}/2}\,\varepsilon(\mathbf{k}+\mathbf{p}_{\mathrm{S}}/2) - \nabla_{\mathbf{k}-\mathbf{p}_{\mathrm{S}}/2}\,\varepsilon(\mathbf{k}-\mathbf{p}_{\mathrm{S}}/2)\right]_{\mathrm{p}}$$
$$\approx \frac{1}{2}\left(\mathbf{p}_{\mathrm{S}}^{\mathrm{p}} \cdot \nabla_{\mathbf{k}}\right)\left(\mathbf{p}_{\mathrm{S}}^{\mathrm{pro}} \cdot \nabla_{\mathbf{k}}\right)\varepsilon(\mathbf{k}) \tag{S26}$$

drives difference-frequency Raman excitations, $\pm(\omega_{\mathrm{p}} - \omega_{\mathrm{pro}})$. $\delta S_{\mathbf{k}}^{\mathrm{R}}(t,\tau)$ can be expanded perturbatively and is proportional to the pump and probe condensate momenta. In the absence of the electromagnetic propagation effects and spatial dependencies discussed in our previous works, these Cooper pair center-of-mass momenta oscillate in time during the pulse without any static components. Recalling that $\Delta \tilde{\rho}_2^{\mathrm{p}}(\mathbf{k})$ mainly oscillates at frequencies $\sim \omega_{\mathrm{H}}$ and $\sim 2\omega_{\mathrm{p}}$ (Fig. S1), we see that this difference-frequency Raman source term resonantly drives pseudo-spin precession at frequencies $\omega = 2\omega_{\mathrm{p}} \pm (\omega_{\mathrm{pro}} - \omega_{\mathrm{p}}) = (2\omega_0 \pm \Delta\omega_{\mathrm{pro}}, -2\omega_0 \pm \omega_0)$ and $\omega = \omega_{\mathrm{H}} \pm (\omega_{\mathrm{pro}} - \omega_{\mathrm{p}}) = (\omega_{\mathrm{H}} \pm \Delta\omega_{\mathrm{pro}}, \pm\omega_0 - \omega_{\mathrm{H}})$ similar to previous works. The first process gives MDC-THz peaks at $\omega = \omega_{\mathrm{p}} \pm (\omega_{\mathrm{pro}} - \omega_{\mathrm{p}})$ (PP and FWM) and $\omega = 2\omega_{\mathrm{p}} + \omega_{\mathrm{pro}}$ (3HG). For strong pump fields such that $\omega_{\mathrm{H}} < 2\omega_{\mathrm{p}}$, new peaks emerge, determined by the field-dependent SC excitation energies $\sim \omega_{\mathrm{H}}$ rather than by the laser frequency (Fig. S1). The latter MDC-THz signals arise from the fifth-order processes $\omega_{\mathrm{H}} + \omega_{\mathrm{pro}} + \omega_{\mathrm{p}} - \omega_{\mathrm{p}}$, $\omega_{\mathrm{H}} - \omega_{\mathrm{pro}} + \omega_{\mathrm{p}} - \omega_{\mathrm{p}}$, $\omega_{\mathrm{H}} - 2\omega_{\mathrm{p}} + \omega_{\mathrm{pro}}$, and $\omega_{\mathrm{H}} + 2\omega_{\mathrm{p}} - \omega_{\mathrm{pro}}$. Figure S3 demonstrates the contributions to these processes to MDC-THz peaks, by plotting $\mathcal{E}_{\mathrm{NL}}(\omega)$ as a function of ω_{τ} for fixed $\omega_t = \omega_{\mathrm{H}} - \omega_0$. The result of our full calculation (shaded area) shows two additional strong peaks, at $\omega_{\tau} = -\omega_H$ and $\omega_{\tau} = 2\omega_0 - \omega_H$, which are generated by the CFWM and CPP seventh-order processes proposed here. Note that the sum-frequency third-order processes described by $\delta S^{(2)}$ have minimal contribution to these peaks. Figure S3 shows the contribution of $\delta S^{(\mathrm{R})}$ by comparing the result of the full calculation (shaded area) with the results obtained by switching off the non-interacting contribution to the Raman source term $\delta S_{\mathbf{k}}^{\mathrm{R}}$ (first term in Eq. (S25), red line) or the vertex correction (second term in Eq. (S25), orange line). The main effect of the vertex correction is an enhancement of the signal, while the non-interacting contribution only slightly modifies the signals. The interaction-induced vertex corrections, Eq. (S25), must therefore be included in order to consistently describe the overall nonlinear contribution in a gauge-invariant way [S2]. The weaker peak centered at $\omega_{\tau} = \omega_0 - \omega_{\mathrm{H}}$ in Fig. S3 comes from the Raman process $(\omega_{\mathrm{H}} - \omega_{\mathrm{p}} - \omega_{\mathrm{pro}}) + \omega_{\mathrm{pro}} = (\omega_{\mathrm{H}} - \omega_0, \omega_0 - \omega_{\mathrm{H}})$. While third- and fifth-order Raman and two-photon nonlinear processes have also been discussed in previous works, the enhanced resolution offered by 2D frequency space allows us to distinguish these conventional coherent nonlinear processes from the light-induced SC correlations leading to new CWM peaks with distinct driving field and temperature dependences, discussed in the main text, whose physical origin is analyzed next. The fifth-order Raman nonlinear processes discussed above are listed in Table S3.

III. Parametric pseudo-spin oscillator driving: Seventh-order responses and higher correlations (CWM)

The third term on the rhs of Eq. (S23) describes parametric driving of pseudo-spin oscillations resulting by the coherent pump–probe modulation of the SC order parameter amplitude, $\delta|\Delta_{\mathrm{pp}}(t,\tau)| = |\Delta_{\mathrm{pp}}(t,\tau)| - |\Delta_{\mathrm{p}}(t,\tau)|$, which is controlled by the coherence time τ. $\delta|\Delta_{\mathrm{pp}}(t,\tau)|$ changes the pseudo-spin oscillation frequencies, described by self-consistently solving Eqs. (S22) and (S23). The parametric driving of the pseudo-spin oscillator results from the modulation of the SC energy gap, which, unlike in semiconductors, is determined by the off-diagonal long range order in the driven non-equilibrium SC state. Figure S4 shows the calculated dynamics and corresponding 2D Fourier transform of $\delta|\Delta_{\mathrm{pp}}(t,\tau)|$. The full result (left column) is compared with the result obtained by setting $\mathbf{p}_{\mathrm{S}} = 0$ in Eq. (S22) (right column). First, the Higgs collective mode contribution to $\delta|\Delta_{\mathrm{pp}}(\omega)|$ is the peak located at $\omega = (\omega_{\mathrm{H}}, -\omega_{\mathrm{H}})$. This Higgs mode contribution arises to order $\mathcal{O}(E_{\mathrm{pro}}^2)$, from the process $\omega_{\mathrm{H}} + \omega_{\mathrm{pro}} - \omega_{\mathrm{pro}}$. For the weak probe fields chosen here, the main contribution to $\delta|\Delta_{\mathrm{pp}}(\omega)|$ in Fig. S4 comes from the Raman processes $\pm(\omega_{\mathrm{H}} - \omega_{\mathrm{p}} - \omega_{\mathrm{pro}})$ (cyan
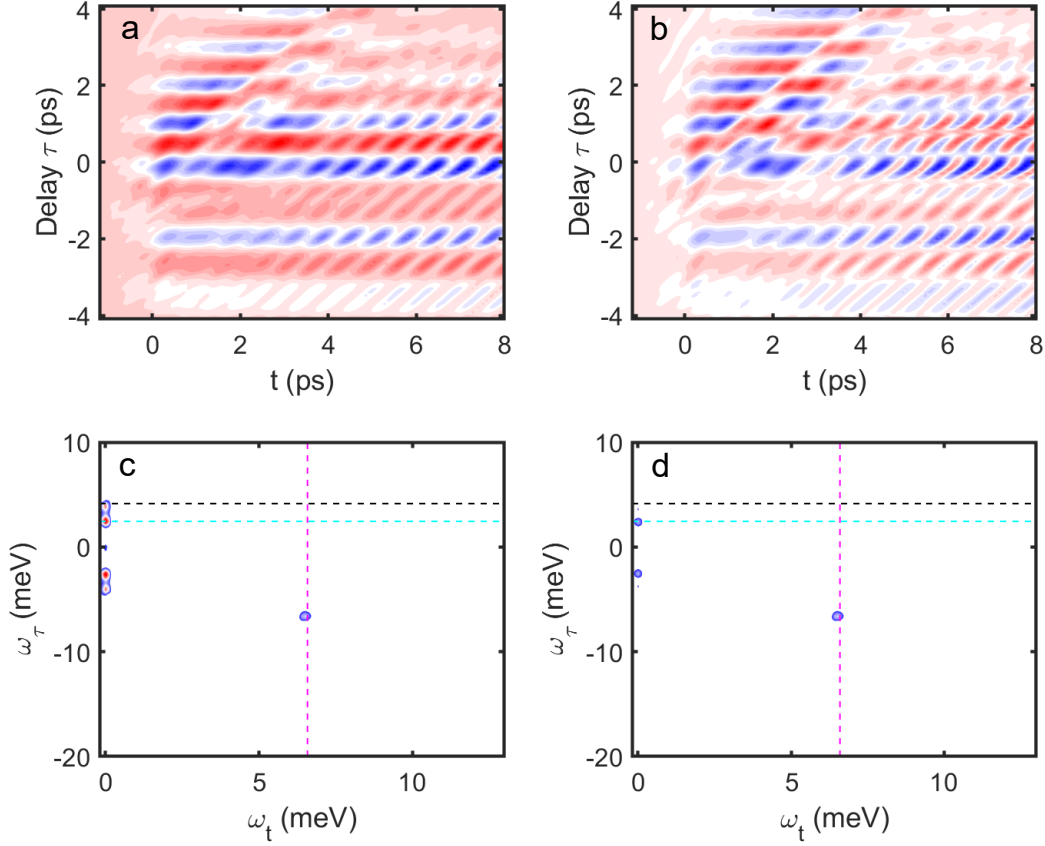
Figure S4. Dynamics and spectra of $\delta\Delta^{\mathrm{PP}}(t,\tau)$. The full result (**a** and **c**) is compared with the result obtained by setting $\mathbf{p}_{\mathrm{S}} = 0$ in Eq. (S22) (**b** and **d**). Vertical dashed line indicates $\omega_t = \omega_{\mathrm{H}}$, while $\omega_\tau = \omega_{\mathrm{H}} - \omega_0$ and $\omega_\tau = \omega_0$ are marked by horizontal dashed cyan and black lines, respectively.

line) and $\pm(2\omega_{\mathrm{p}} - \omega_{\mathrm{p}} - \omega_{\mathrm{pro}})$ (black line). The latter two processes manifest themselves as two separate satellite peaks in the Fourier transform of Fig. S4, located at $\omega_t \sim 0$. For the fields considered here, these peaks in $\delta|\Delta_{\mathrm{pp}}(\omega)|$ can be described by expanding Eq. (S22) to order $\mathcal{O}(\mathbf{p}_{\mathrm{S}}^2)$, which gives a coherent nonlinear coupling between ω_{H} and $\omega_{\mathrm{H}} - \omega_{\mathrm{p}} - \omega_{\mathrm{pro}}$. The first process, $\pm(\omega_{\mathrm{pro}} + \omega_{\mathrm{p}} - \omega_{\mathrm{H}}) = \pm(2\omega_0 - \omega_{\mathrm{H}} \pm \Delta\omega_{\mathrm{pro}}, \omega_{\mathrm{H}} - \omega_0)$ (cyan line), is described by the second term on the rhs of Eq. (S22). The first term on the rhs of Eq. (S22) also contributes to this peak via the higher order process $\pm(\omega_{\mathrm{H}} + \omega_{\mathrm{p}} - \omega_{\mathrm{pro}} - 2\omega_{\mathrm{p}})$. The second process, $\pm(2\omega_{\mathrm{p}} - \omega_{\mathrm{pro}} - \omega_{\mathrm{p}}) = \pm(\Delta\omega_{\mathrm{pro}}, \omega_0)$, arises from the second term in Eq. (S22) and leads to a slightly smaller peak in Fig. S4 (black line). We conclude that the main contribution to the coherent order parameter modulation $\delta|\Delta_{\mathrm{pp}}(t,\tau)|$ arises from the difference-frequency nonlinear process involving a Higgs or QP coherence $\Delta\tilde{\rho}_2^{\mathrm{p}}$ (ω_{H} or $2\omega_p$ SC excitation) and a two-photon excitation $\omega_{\mathrm{p}} + \omega_{\mathrm{pro}}$ controlled by the coherence time τ. The above difference-frequency nonlinear Raman processes are analogous to the coherent exciton population photogeneration process that determines the exciton–exciton interaction coherent signal in semiconductors [S11, S12], or the photogeneration of collective excitations that determines the coherent signal of the two-dimensional electron gas [S15, S16]. While the photogeneration of coherent exciton populations is a second order process, here coherent order parameter modulation is a fourth-order process, since it involves creation and annihilation of two-photon SC excitations. Coherent control of the SC order parameter via τ manifests itself via the shift of the $\omega_t \sim 0$ spectral peaks along the vertical ω_τ axis, by $\omega_\tau = \pm(\omega_{\mathrm{H}} - \omega_0)$ and $\omega_\tau = \pm\omega_0$ in Fig. S4.

To interpret the contributions to MDC-THz coming from such SC order parameter pump–probe coherent modulation, we stress that, for weak probe, the relevant source term on the rhs of Eq. (S23) is $\propto \Delta\tilde{\rho}_2^{\mathrm{p}} \, \delta|\Delta_{\mathrm{pp}}|$. Unlike for the Raman processes driven by $\delta S^{(2)}$ and $\delta S^{(R)}$, which follow the laser pulse time dependence (Eqs. (S24) and (S26)), the contribution of $\Delta\tilde{\rho}_2^{\mathrm{p}} \, \delta|\Delta_{\mathrm{pp}}|$ is determined by the coupling of all $\mathbf{k}$-state pseudo-spins by the pairing interaction. While

such collective effects also give rise to the Higgs elementary excitation, here they enhance the nonlinear response determined via light-induced interactions between different elementary excitations. This interaction-induced highly nonlinear signal may be thought of as analogous to the interaction of the exciton polarization P with the coherent population grating δn, which describes the $\propto P\delta n$ exciton–exciton interaction signal in semiconductors. Similarly here, $\Delta\tilde{\rho}_2^{\mathrm{p}}\,\delta|\Delta_{\mathrm{pp}}|$ describes the interaction of an elementary excitation of the pump-driven state, $\Delta\tilde{\rho}_2^{\mathrm{p}}$, with the SC excitation in $\delta|\Delta_{\mathrm{pp}}|$, Eq. (S22). Importantly, the distinct temperature and field dependence of $\delta|\Delta_{\mathrm{pp}}|$ leads to distinct behavior of the MDC-THz peaks generated by this term (Fig. 3). Note that the last term in Eq. (S23) also originates from collective effects (Higgs mode), whose role is discussed in the next section.

$\Delta\tilde{\rho}_2^{\mathrm{p}}\,\delta|\Delta_{\mathrm{pp}}|$ drives $\delta\tilde{\rho}_2^{\mathrm{pp}}(\mathbf{k},\omega)$ via the sixth-order processes $2\omega_{\mathrm{p}}\pm(\omega_{\mathrm{pro}}+\omega_{\mathrm{p}}-\omega_{\mathrm{H}})$, $\omega_{\mathrm{H}}\pm(\omega_{\mathrm{pro}}+\omega_{\mathrm{p}}-\omega_{\mathrm{H}})$, $2\omega_{\mathrm{p}}\pm(\omega_{\mathrm{pro}}+\omega_{\mathrm{p}}-2\omega_{\mathrm{p}})$, and $\omega_{\mathrm{H}}\pm(\omega_{\mathrm{pro}}+\omega_{\mathrm{p}}-2\omega_{\mathrm{p}})$. The above nonlinear processes involve correlations between *two* pump-driven SC excitations, Higgs or QP (ω_{H} or $2\omega_{\mathrm{p}}$), and a two-photon excitation $\omega_{\mathrm{pro}}+\omega_{\mathrm{p}}$. In contrast, $\delta S^{(2)}$ involves a sum-frequency excitation $\omega_{\mathrm{pro}}+\omega_{\mathrm{p}}$ (Eq. (S24)) and $\delta S^{(\mathrm{R})}$ involves a single SC excitation (ω_{H} or $2\omega_{\mathrm{p}}$) coupled with a difference-frequency Raman excitation $\pm(\omega_{\mathrm{pro}}-\omega_{\mathrm{p}})$. From the third term on the rhs of Eq. (S20), we obtain that $\Delta\tilde{\rho}_2^{\mathrm{p}}\,\delta|\Delta_{\mathrm{pp}}|$ generates MDC-THz peaks in Fig. 2g close to PP frequencies, $\omega_{\mathrm{pro}}+(2\omega_{\mathrm{p}}-\omega_{\mathrm{H}})+(\omega_{\mathrm{p}}-\omega_{\mathrm{p}})$ and $\omega_{\mathrm{pro}}+(\omega_{\mathrm{H}}-\omega_{\mathrm{H}})+(\omega_{\mathrm{p}}-\omega_{\mathrm{p}})$, 3HG frequencies, $2\omega_{\mathrm{p}}+\omega_{\mathrm{pro}}+(2\omega_{\mathrm{p}}-\omega_{\mathrm{H}})$ and $2\omega_{\mathrm{p}}+\omega_{\mathrm{pro}}+(\omega_{\mathrm{H}}-\omega_{\mathrm{H}})$, and FWM frequencies, $\omega_{\mathrm{H}}-\omega_{\mathrm{pro}}+(2\omega_{\mathrm{p}}-2\omega_{\mathrm{p}})$ and $\omega_{\mathrm{H}}-\omega_{\mathrm{pro}}+\omega_{\mathrm{H}}-2\omega_{\mathrm{p}}$. For sufficiently high driving fields, the above higher correlation processes dominate the conventional FWM, PP, and 3HG signals. This is clearly seen in Fig. S3, which shows the spectrum as a function of ω_τ at the FWM frequency $\omega_t=\omega_{\mathrm{H}}-\omega_0$ (compare the results in Fig. S3 with those obtained for $\delta|\Delta_{\mathrm{pp}}|=0$, purple line). Most important, however, for distinguishing the proposed light-induced higher correlation processes experimentally is that that they lead to new CWM peaks at frequencies where there is no contribution for weak driving fields. In particular, strong CWM peaks are clearly seen in Figs. 2f and g, at $2\omega_{\mathrm{p}}+\omega_{\mathrm{H}}-\omega_{\mathrm{pro}}+(\omega_{\mathrm{p}}-\omega_{\mathrm{p}})$ (strong CWM peak) and at $2\omega_{\mathrm{H}}-\omega_{\mathrm{pro}}+(\omega_{\mathrm{p}}-\omega_{\mathrm{p}})$ (weaker CWM peak). These new CWM peaks are located at $\omega_t\sim\omega_{\mathrm{H}}+\omega_0$ and $2\omega_{\mathrm{H}}-\omega_0$, which is comparable to the frequency ω_t corresponding to 3HG processes. However, the CWM peaks are well separated from the 3HG peaks along the vertical ω_τ axis, by the field-dependent $\omega_\tau=-2\omega_0-\omega_{\mathrm{H}}$ and $\omega_\tau=-2\omega_{\mathrm{H}}$. This shift along the axis corresponding to the coherence time provides a clear experimental prediction of how to observe higher correlations in the MDC-THz spectra. Finally, weaker peaks are also observed at $\omega_{\mathrm{H}}+\omega_{\mathrm{pro}}+2\omega_p-2\omega_{\mathrm{p}}$ and $\omega_{\mathrm{pro}}+\omega_{\mathrm{H}}-2\omega_{\mathrm{p}}+\omega_{\mathrm{p}}-\omega_{\mathrm{p}}$. We conclude that MDC-THz for phase-locked pump–probe THz pulses and 2D frequency space provide super-resolution for imaging light-driven SC quantum states controlled via the relative phase of the two electromagnetic fields. All seventh-order nonlinear processes discussed above are summarized in Table S4.

IV. Inversion-Symmetry-Forbidden Nonlinear Responses (ISWM)

The difference-frequency Raman pump–probe processes $\pm(\omega_{\mathrm{p}}-\omega_{\mathrm{pro}})$ become directly observable in the MDC-THz spectra when the THz dynamical breaking of inversion symmetry persists after the pulse. The theoretical prediction of equilibrium-symmetry-forbidden spectral peaks above critical driving field when electromagnetic propagation effects are included to break IS was confirmed experimentally [S5, S6]. In particular, we have already showed, by using the theory of Ref. [S2], that THz dynamical breaking of inversion symmetry arises from difference-frequency Raman coherent nonlinear processes when light-wave electromagnetic propagation effects inside a thin SC film are included in the calculation. Figure 4 shows the MDC-THz spectra obtained in this way. Electromagnetic propagation inside the nonlinear SC medium results in the coherent photogeneration of a symmetry-breaking nonlinear dc supercurrent through difference-frequency Raman processes. This dc nonlinear photocurrent is controlled coherently via the dynamical interplay of pump-induced nonlinear response with light-wave propagation inside the SC system. Electromagnetic propagation inside the thin SC film is included in our calculation by self-consistently solving Maxwell's equations and the gauge-invariant SC Bloch equations [S2]. The photogenerated dc supercurrent results in a $\omega=0$ component of $\mathbf{p}_{\mathrm{S}}^{\mathrm{p}}$, in addition to the ω_0 frequency in Eq. (S20), which persists well after the pulse in the realistic system. As a result of such persisting inversion symmetry breaking, the Raman processes assisted by SC excitations, discussed above, lead to new symmetry-forbidden seventh-order wave-mixing peaks in the MDC-THz spectra (ISWM). The latter are separated in 2D frequency space from the rest of the peaks. In particular, with photoinduced inversion symmetry breaking (IS), we obtain MDC-THz peaks at new frequencies $\omega=\omega_{\mathrm{H}}\pm(\omega_{\mathrm{pro}}-\omega_{\mathrm{p}})=(\omega_{\mathrm{H}}\pm\Delta\omega_{\mathrm{pro}},\pm\omega_0-\omega_{\mathrm{H}})$ and $\omega=(\omega_{\mathrm{H}},-\omega_{\mathrm{H}})$. These even-order nonlinearity MDC-THz peaks are forbidden by the equilibrium symmetry, but are clearly observed in the calculation of Fig. 4, where electromagnetic propagation effects are included. The dominant IS MDC-THz peaks are listed in Table S5.

The above seventh-order wave-mixing processes directly reflect the Higgs collective mode. The latter uniquely identifies a SC state, similar to the Meissner effect. As a result, the observation of wave-mixing peaks at $\omega_t=\omega_{\mathrm{H}}$,

including sidebands along the ω_τ vertical axis, which can be used as the basis of a quantum sensor of non-equilibrium superconductivity, with the super-resolution offered by MDC-THz imaging of quantum states.

Supplementary Note 4: High-order Correlation Contributions to the MDC-THz spectra

In this section, we summarize and distinguish between all the different processes that contribute to the MDC-THz spectra, by separating their contributions in 2D frequency space to achieve super-resolution imaging of non-equilibrium SC quantum states. While many different processes contribute at the same frequency, ω_t the second frequency, ω_τ, introduced by the pump–probe electromagnetic field relative phase allows us to separate and distinguish them. First, we list the pump–probe (PP), four-wave-mixing (FWM) and third harmonic generation (3HG) nonlinear processes previously discussed in the SC literature, which also contribute in semiconductor systems:

signal	nonlinear process	frequency space
PP	$\omega_\mathrm{p} - \omega_\mathrm{p} + \omega_\mathrm{pro}$	$(\omega_0, 0)$
PP	$\omega_\mathrm{pro} - \omega_\mathrm{pro} + \omega_\mathrm{p}$	$(\omega_0, -\omega_0)$
FWM	$2\omega_\mathrm{p} - \omega_\mathrm{pro}$	$(\omega_0, -2\omega_0)$
FWM	$2\omega_\mathrm{pro} - \omega_\mathrm{p}$	(ω_0, ω_0)
3HG	$2\omega_\mathrm{pro} + \omega_\mathrm{p}$	$(3\omega_0, -\omega_0)$
3HG	$2\omega_\mathrm{p} + \omega_\mathrm{pro}$	$(3\omega_0, -2\omega_0)$

Table S1. Third-order nonlinear processes.

Next we summarize the third-order signals which separate from the above signals when the excitation energy gap, $\omega_\mathrm{H} = 2\Delta_\infty < 2\omega_0 \sim 2\Delta_0$, shifts with increasing pump field, as is the case in superconductors:

signal	nonlinear process	frequency space
FWM	$\omega_\mathrm{H} - \omega_\mathrm{pro}$	$(\omega_\mathrm{H} - \omega_0, -\omega_\mathrm{H})$
3HG	$\omega_\mathrm{H} + \omega_\mathrm{pro}$	$(\omega_\mathrm{H} + \omega_0, -\omega_\mathrm{H})$

Table S2. Third-order signals for $\omega_\mathrm{H} < 2\omega_0$.

The difference-frequency-Raman process described by $\delta S_\mathbf{k}^\mathrm{R}$ leads to the fifth-order signals:

signal	nonlinear process	frequency space
PP	$(\omega_\mathrm{H} - 2\omega_\mathrm{p}) + \omega_\mathrm{pro}$	$(\omega_\mathrm{H} - \omega_0, -\omega_\mathrm{H} + 2\omega_0)$
FWM	$\omega_\mathrm{H} - \omega_\mathrm{pro} + (\omega_\mathrm{p} - \omega_\mathrm{p})$	$(\omega_\mathrm{H} - \omega_0, -\omega_\mathrm{H})$
3HG	$\omega_\mathrm{H} + \omega_\mathrm{pro} + (\omega_\mathrm{p} - \omega_\mathrm{p})$	$(\omega_\mathrm{H} + \omega_0, -\omega_\mathrm{H})$
WM	$\omega_\mathrm{H} + 2\omega_\mathrm{p} - \omega_\mathrm{pro}$	$(\omega_\mathrm{H} + \omega_0, -\omega_\mathrm{H} - 2\omega_0)$

Table S3. Fifth-order signals.

Next we summarize the main result of this paper: seventh-order correlation processes photogenerated by parametric driving of the Anderson pseudo-spin oscillators by pump–probe coherent modulation of the SC order parameter. These processes lead to strong CWM peaks discovered theoretically here, which dominate over the third-order and fifth-order signals summarized above for strong pump fields, when $\omega_\mathrm{H} < 2\Delta_0$. Unlike for the previously discussed nonlinear signals, the above seventh-order nonlinear responses are determined by interactions between two SC excitations (QP and Higgs), which dominate above critical pump driving over the single-excitation dynamics that generates the third- and fifth-order responses.

signal	nonlinear process	frequency space
CPP	$(\omega_{\mathrm{H}} - 2\omega_{\mathrm{p}}) + (\omega_{\mathrm{p}} - \omega_{\mathrm{p}}) + \omega_{\mathrm{pro}}$	$(\omega_{\mathrm{H}} - \omega_0, -\omega_{\mathrm{H}} + 2\omega_0)$
CPP	$(\omega_{\mathrm{H}} - \omega_{\mathrm{H}}) + (\omega_{\mathrm{p}} - \omega_{\mathrm{p}}) + \omega_{\mathrm{pro}}$	$(\omega_0, 0)$
CFWM	$(\omega_{\mathrm{H}} - 2\omega_{\mathrm{p}}) + 2\omega_{\mathrm{p}} - \omega_{\mathrm{pro}}$	$(\omega_{\mathrm{H}} - \omega_0, -\omega_{\mathrm{H}})$
CFWM	$(\omega_{\mathrm{H}} - 2\omega_{\mathrm{p}}) + \omega_{\mathrm{H}} - \omega_{\mathrm{pro}}$	$(2\omega_{\mathrm{H}} - 3\omega_0, -2\omega_{\mathrm{H}} + 2\omega_0)$
C3HG	$(\omega_{\mathrm{H}} - 2\omega_{\mathrm{p}}) + 2\omega_{\mathrm{p}} + \omega_{\mathrm{pro}}$	$(\omega_{\mathrm{H}} + \omega_0, -\omega_{\mathrm{H}})$
C3HG	$(\omega_{\mathrm{H}} - \omega_{\mathrm{H}}) + 2\omega_{\mathrm{p}} + \omega_{\mathrm{pro}}$	$(3\omega_0, -2\omega_0)$
CWM	$\omega_{\mathrm{H}} + 2\omega_{\mathrm{p}} + (\omega_{\mathrm{p}} - \omega_{\mathrm{p}}) - \omega_{\mathrm{pro}}$	$(\omega_{\mathrm{H}} + \omega_0, -\omega_{\mathrm{H}} - 2\omega_0)$
CWM	$2\omega_{\mathrm{H}} + (\omega_{\mathrm{p}} - \omega_{\mathrm{p}}) - \omega_{\mathrm{pro}}$	$(2\omega_{\mathrm{H}} - \omega_0, -2\omega_{\mathrm{H}})$

Table S4. Seventh-order correlation processes.

Finally, the following seventh-order processes, which contribute when light-induced inversion symmetry breaking persists after the pulses, lead to new wave-mixing peaks at symmetry-forbidden frequencies (ISWM):

signal	nonlinear process	frequency space
ISWM	$(\omega_{\mathrm{H}} - 2\omega_{\mathrm{p}}) + \omega_{\mathrm{p}} + \omega_{\mathrm{pro}}$	$(\omega_{\mathrm{H}}, -\omega_{\mathrm{H}} + \omega_0)$
ISWM	$\omega_{\mathrm{H}} + (\omega_{\mathrm{p}} - \omega_{\mathrm{p}}) + (\omega_{\mathrm{pro}} - \omega_{\mathrm{pro}})$	$(\omega_{\mathrm{H}}, -\omega_{\mathrm{H}})$
ISWM	$\omega_{\mathrm{H}} + \omega_{\mathrm{p}} + (\omega_{\mathrm{p}} - \omega_{\mathrm{p}}) - \omega_{\mathrm{pro}}$	$(\omega_{\mathrm{H}}, -\omega_{\mathrm{H}} - \omega_0)$

Table S5. IS wave-mixing signals.

These seventh-order wave-mixing peaks at $\omega_t = \omega_{\mathrm{H}}$ represent direct signatures of the Higgs collective mode, which characterizes non-equilibrium superconductivity in ways that become possible due to dynamical symmetry breaking by light-wave electromagnetic propagation inside the SC sample. In particular, observation of these Higgs ISWM peaks presents direct evidence of a moving condensate light-driven non-equilibrium SC state. We conclude that the super-resolution offered by the MDC-THz spectra calculated here provides a sensor of light-induced correlations in non-equilibrium quantum states.

Supplementary References

S1. Stephen, M. J. Transport equations for superconductors. *Phys. Rev.* **139**, A197–A205 (1965).

S2. Mootz, M., Wang, J. & Perakis, I. E. Lightwave terahertz quantum manipulation of nonequilibrium superconductor phases and their collective modes. *Phys. Rev. B* **102**, 054517 (2020).

S3. Anderson, P. W. Random-phase approximation in the theory of superconductivity. *Phys. Rev.* **112**, 1900–1916 (1958).

S4. Yang, X. *et al.* Terahertz-light quantum tuning of a metastable emergent phase hidden by superconductivity. *Nat. Mater.* **17**, 586 (2018).

S5. Yang, X. *et al.* Lightwave-driven gapless superconductivity and forbidden quantum beats by terahertz symmetry breaking. *Nat. Photon.* **13**, 707–713 (2019).

S6. Vaswani, C. *et al.* Terahertz second-harmonic generation from lightwave acceleration of symmetry-breaking nonlinear supercurrents. *Phys. Rev. Lett.* **124**, 207003 (2020).

S7. Tsuji, N. & Aoki, H. Theory of anderson pseudo-spin resonance with Higgs mode in superconductors. *Phys. Rev. B* **92**, 064508 (2015).

S8. Cea, T., Castellani, C. & Benfatto, L. Nonlinear optical effects and third-harmonic generation in superconductors: Cooper pairs versus Higgs mode contribution. *Phys. Rev. B* **93**, 180507 (2016).

S9. Udina, M., Cea, T. & Benfatto, L. Theory of coherent-oscillations generation in terahertz pump-probe spectroscopy: From phonons to electronic collective modes. *Phys. Rev. B* **100**, 165131 (2019).

S10. Mukamel, S. *Principles of nonlinear optical spectroscopy.* 6 (Oxford University Press on Demand, 1999).

S11. Schmitt-Rink, S. & Chemla, D. S. Collective excitations and the dynamical Stark effect in a coherently driven exciton system. *Phys. Rev. Lett.* **57**, 2752–2755 (1986).

S12. Wegener, M., Chemla, D. S., Schmitt-Rink, S. & Schäfer, W. Line shape of time-resolved four-wave mixing. *Phys. Rev. A* **42**, 5675–5683 (1990).

S13. Vaswani, C. *et al.* Light quantum control of persisting Higgs modes in iron-based superconductors. *Nat. Commun.* **12**, 258 (2021).

S14. Shahbazyan, T. V., Primozich, N., Perakis, I. E. & Chemla, D. S. Femtosecond coherent dynamics of the Fermi-edge singularity and exciton hybrid. *Phys. Rev. Lett.* **84**, 2006–2009 (2000).

S15. Karadimitriou, M. E., Kavousanaki, E. G., Dani, K. M., Fromer, N. A. & Perakis, I. E. Strong electronic correlation effects in coherent multidimensional nonlinear optical spectroscopy. *J. Phys. Chem. B* **115**, 5634–5647 (2011).

S16. Fromer, N. A. *et al.* Dynamics of inter-Landau-level excitations of a two-dimensional electron gas in the quantum hall regime. *Phys. Rev. Lett.* **89**, 067401 (2002).